1   # Retrieval Algorithm for Aerosol Effective Height from the

2   # Geostationary Environment Monitoring Spectrometer (GEMS)

4   Sang Seo Park[1,*], Jhoon Kim[2], Yeseul Cho[2], Hanlim Lee[3], Junsung Park[3], Dong-Won

5   Lee[4], Won-Jin Lee[4], Deok-Rae Kim[4]

6   *[1] Department of Urban and Environmental Engineering, Ulsan National Institute of Science*

7   *and Technology, Ulsan, Korea*

8   *[2]Department of Atmospheric Sciences, Yonsei University, Seoul, Korea*

9   *[3]Division of Earth and Environmental System Sciences, Pukyong National University, Busan,*

10   *South Korea*

11   *[4]Envionment Satellite Center, National Institute of Environmental Research, Incheon, Korea*

15   *Corresponding author. Sang Seo Park (sangseopark@unist.ac.kr)

18   Submitted to Atmospheric Measurement Techniques

19   2023. 06.

Abstract

An algorithm for aerosol effective height (AEH) was developed for operational use with observations from the Geostationary Environment Monitoring Spectrometer (GEMS). The retrieval technique uses the slant column density of the oxygen dimer (O_2-O_2) at 477 nm, which is converted into AEH after retrieval of aerosol and surface optical properties from GEMS operational algorithms. The AEH retrieval results show significant AEH values and continuously monitor aerosol vertical height information in severe dust plumes over East Asia, and the collection of plume height information for anthropogenic aerosol pollutants over India. Compared to the AEH retrieved from Cloud-Aerosol Lidar with Orthogonal Polarization (CALIOP), the retrieval results show insignificant bias with a standard deviation of 1.4 km for the AEH difference over the GEMS observation domain from January to June 2021 due to uncertainty in input parameters for aerosol and surface. The AEH difference depends on aerosol optical properties and surface albedo. Compared to the aerosol layer height obtained from the tropospheric monitoring instrument (TROPOMI), differences of 0.78 ± 0.81 and 1.16 ± 0.92 km were obtained for pixels with single scattering albedo (SSA) < 0.90 and 0.90 < SSA < 0.95, respectively, with significant dependence on aerosol type.

Keywords: aerosol effective height, aerosol optical depth, environmental satellite, GEMS

1. Introduction

Since the launch of the Total Ozone Mapping Spectrometer (TOMS) on Nimbus-7, ultraviolet (UV)-visible satellite measurements have been used for environmental monitoring of the distribution and reaction processes of pollutants (e.g., anthropogenic aerosols, tropospheric ozone, NO_2, and SO_2). Measurements from environmental satellites have been used to estimate gaseous species in the atmosphere, resulting in vertical column integrated amounts. However, these column-integrated amounts and associated surface concentrations have uncertainty due to simultaneous changes in optical path length associated with the vertical distribution of target species and amounts of scattering materials (clouds and aerosols) present.

Environmental satellite sensors, in particular those that measure UV-visible wavelength range, have been used to detect aerosol and cloud signals by using the aerosol index (e.g., Buchard *et al.*, 2015; Herman *et al.*, 1997; Torres *et al.*, 1998, 2002; Prospero *et al.*, 2000; de Graaf *et al.*, 2005) and scattering radiative index values (Penning de Vries *et al.*, 2009, 2015; Kooreman *et al.*, 2020; Kim *et al.*, 2018), although these indices only have qualitative characteristics and limitations to identify aerosol amounts. In addition, measurements of scattering material amounts, such as aerosol optical depth (AOD) and radiative cloud fraction, have also been retrieved from pixel-based radiance data in UV-visible wavelength range. Recently, various aerosol retrieval algorithms have been developed for use with satellite sensors. These algorithms focus on improved trace gas retrieval as well as direct monitoring of aerosol properties, such as AOD and single scattering albedo (SSA) (e.g., Ahn *et al.*, 2014; Kim *et al.*, 2020; Torres et al., 2020).

Although the algorithms developed for environmental satellite sensors indicate the

68 presence and amount of scattering materials, the accuracy of these retrieval algorithms

69 for trace gases is significantly affected by the relative vertical distributions between

70 trace gases and scattering materials (e.g., Lorente *et al.*, 2017; Hong *et al.*, 2017). For

71 this reason, estimating cloud and aerosol vertical parameters is very important. For

72 cloud vertical information, cloud height information has been estimated simultaneously

73 with cloud optical depth and radiative cloud fraction data using the rotational Raman

74 scattering (Joiner and Vasilkov, 2006; Vasilkov *et al.*, 2008; Joiner and Bhartia, 1995)

75 and absorption intensity of the oxygen dimer (O_2-O_2) (Accarreta *et al.*, 2004; Vasilkov

76 *et al.*, 2018; Choi *et al.*, 2021) combined with normalized radiance. Similarly, the

77 aerosol vertical distribution can be estimated using the oxygen absorption bands, such

78 as the O_2-O_2 (Park *et al.*, 2016; Chimot *et al.*, 2017; Choi *et al.*, 2019, 2020), O_2-A

79 (Dubisson *et al.*, 2009; Geddes and Boesch, 2015; Sanders *et al.*, 2015; Zeng *et al.*,

80 2020), and O_2-B (Ding *et al.*, 2016) bands, as well as combinations of these bands

81 (Sanghavi *et al.*, 2012; Chen et al., 2021). In addition, an algorithm for aerosol vertical

82 information has been developed based on hyperspectral UV-visible radiance from

83 satellite observation. Nanda *et al.* (2018) demonstrated the possibility of aerosol height

84 retrieval from the O_2-A band developed an algorithm using Tropospheric Monitoring

85 Instrument (TROPOMI) (Sanders and de Haan, 2016; Nanda *et al.*, 2020) and

86 implemented the algorithm operationally.

87 However, the vertical distribution of aerosol is difficult to assess because of its large

88 spatio-temporal variability. Although the Cloud-Aerosol Lidar with Orthogonal

89 Polarization (CALIOP) provided the aerosol vertical distribution with high vertical

90 resolution (Omar et al., 2009), other satellites for passive sensors are only able to

91 estimate the representative parameter of aerosol height. Veihelmann et al. (2007)

92   showed that the number of degrees of freedom of signal for aerosol is 2~4 for most of

93   satellite observation conditions by the ozone monitoring instrument (OMI). It means

94   that the number of information for aerosol vertical distribution have a limitation.

95   Because of limitation for describing the aerosol vertical information, aerosol layer

96   height (ALH) (Nanda et al., 2018) or aerosol effective height (AEH) (Park et al., 2016)

97   were defined to retrieve the aerosol vertical information from the passive satellite

98   sensors.

99   The Geostationary Environment Monitoring Spectrometer (GEMS), which was

100   launched by South Korea in February 2020, retrieves data related to major trace gases

101   and aerosol properties (Kim *et al.*, 2020). The main purpose of GEMS is to monitor air

102   quality, and aerosol properties are targets of such monitoring over East Asia. For this

103   reason, the GEMS aerosol algorithm was developed as multiple operational products.

104   Aerosol properties are obtained for the purposes of monitoring surface air quality and

105   aerosol effects for the air mass factor (AMF) calculation. In addition to the aerosol

106   optical property algorithm, the GEMS aerosol product is additionally applied to the

107   aerosol vertical information, AEH. For the possibility for development of an AEH

108   retrieval algorithm, Park *et al.* (2016) conducted theoretical sensitivity testing of AEH

109   retrieval using solely the O_2-O_2 absorption band along with aerosol and surface

110   properties. Overall, the sensitivity of AEH retrieval was strongly affected by SSA, AOD,

111   and aerosol types including optical and size properties, and the error budget for AEH

112   retrieval using the O_2-O_2 band was 739 ~ 1276 m. In addition, case studies of AEH

113   during dust transport over East Asia were conducted using radiance data from the Ozone

114   Monitoring Instrument (OMI) and aerosol optical properties from the Moderate

115   Resolution Imaging Spectroradiometer (MODIS).

116   Based on theoretical considerations and case results of previous studies, we introduce

117   an operational retrieval algorithm for AEH. Section 2 describes the details of the AEH

118   retrieval algorithm for GEMS and provides a list of the detailed input parameters.

119   Section 3 introduces the details of satellite sensors for the comparison and validation in

120   this study. Section 4 reports retrieval results based on case studies of aerosol transport,

121   and section 5 contains validation results based on Cloud-Aerosol Lidar with Orthogonal

122   Polarization (CALIOP) and TROPOMI data. Finally, we show conclusion and summary

123   in section 6.

124

125   **2. AEH retrieval algorithm**

126   AEH is a layer height parameter that considers the penetration of photons into the

127   aerosol layer. In this study, the AEH product from GEMS is defined as the height with

128   aerosol extinction integrated from the surface of $(1\text{-}exp^{-1}) \times$ AOD, and a detailed

129   definition of AEH was introduced by Park $et\ al.$ (2016). Numerous previous studies

130   have used the aerosol top layer height (Kohkanovsky and Rozanov, 2010) or middle

131   layer height (i.e. ALH) (e.g., Sanders $et\ al.$, 2015; Nanda $et\ al.$, 2020) as the aerosol

132   vertical layer parameter. AEH is similar to the aerosol top layer height but with a slight

133   bias. For AEH retrieval, the vertical distribution assumption is also important. The

134   Gaussian Density Fitting (GDF) distribution, which is a modified Gaussian distribution

135   structure, is assumed for AEH retrieval. The full-width at half-maximum (FWHM) of

136   the aerosol layer is 1 km. Based on the assumptions about the aerosol vertical

137   distribution, the AEH value is greater than the peak height of the Gaussian distribution

138   and lower than the aerosol top layer height. Detailed description of AEH and other

139   aerosol vertical parameters are shown in Figure 1.

140

141   **Figure 1.** Description of difference between AEH and ALH in idealized aerosol

142   vertical distribution.

143

144   **Figure 2.** Flowchart of the AEH retrieval algorithm for GEMS satellite observation.

145

146   Figure 2 shows the overall flowchart of the AEH algorithm for GEMS satellite. The

147   GEMS is onboard the Geostationary Korea multipurpose satellite 2B (GK2B) as

148   orbiting at 128.2°E, and scans from 145°E to 75°E with north-south coverage of

149   5°S~45°N. The GK2B observation schedule shares the GEMS and the Geostationary

150   Ocean Color Imager 2 (GOCI2). For this reason, the GEMS scan the 30 minutes

151   duration from every hour from 45 minutes to 15 minutes during daytime. The standard

152   spatial resolution of GEMS is 7×8 km. The spectral resolution and sampling are

153   respectively 0.6 nm with full-width and half-maximum (FWHM) and 0.2 nm with

154   spectral range of 300~500 nm. Because the spectral coverage is limited to 300-500 nm,

155   the AEH from GEMS is applied to the O_2-O_2 absorption band. In AEH estimation, other

156   aerosol characteristics, including aerosol amounts and optical properties, affect retrieval

157   accuracy.

158   The GEMS Level 2 aerosol operational algorithm (L2AERAOD) retrieves the aerosol

159   index (AI) values for UV and visible wavelengths, as well as AOD and SSA with

160   considering the aerosol types (National Institute of Environmental Research, 2020a).

161   The aerosol types are defined as absorbing, non-absorbing, and dust types by using the

162   classification methods based on the UV and visible AIs (e.g., Go et al., 2020). Park *et al.*

163   (2016) noted that the error budget of AEH is significantly affected by uncertainty in

164   AOD and SSA and by the misclassification of aerosol types, which is directly related to

165   the optical property and size information. Main error sources for AEH retrieval can be

166   obtained from the L2AERAOD results. Therefore, the L2AERAOD results for AOD

167   and SSA at 550 nm were adopted as input data for aerosol properties.

168   Although L2AERAOD retrieved their own surface reflectance for accurate separation

169   of surface signals from total reflectance at the top of the atmosphere (TOA), the

170 standard product for surface reflectance (L2SFC) (National Institute of Environmental

171 Research, 2020b) was also independently retrieved from GEMS radiance/irradiance data

172 with specific temporal periods. L2SFC is the reference product for spectral surface

173 reflectance. The L2SFC retrieves the surface reflectivity in multiple spectral channels,

174 and retrieves the black surface reflectivity (BSR) and bi-directional reflectance

175 distribution function (BRDF) based on the original pixel resolution. L2SFC was used as

176 reference data for the surface products for all trace gas retrieval algorithms. Similarly,

177 the AEH retrieval algorithm also uses L2SFC as a reference surface property in

178 operation. Specifically, the BSR value at 477 nm is used as the surface reflectance input

179 for AEH retrieval.

180 **Table 1.** Details of fitting parameter for O_2-O_2 SCD estimation via the DOAS method.

Parameter	
Fitting window	460 – 486 nm
Absorption cross section	NO_2 at 220 and 294 K (Vandaele *et al.*, 1998)
	O_3 at 223, 243 and 293K (Bogumil *et al.*, 2001)
	O_2-O_2 at 293 K (Thalman and Volkamer, 2013)
	Ring

181 For AEH retrieval, the basic method is the identification of changes in optical path

182 length caused by effective aerosol layer height variation. To measure the optical path

183 length change, O_2-O_2 slant column density (SCD) retrieved by the differential optical

184 absorption spectroscopy (DOAS) method was used. In the GEMS product, the O_2-O_2

185 SCD at 477 nm absorption band is most useful absorption band because this absorption

186 band is strongest absorption band within the GEMS spectral observation range. Detailed

187 DOAS fitting parameter and setting information is provided in Table 1 for the

188 estimation of O_2-O_2 SCD from both the simulation and observation data. For the O_2-O_2

189 SCD estimation at 477 nm, the fitting window is ranged from 460 to 486 nm to cover

190 the full absorption structure of O_2-O_2. Within the fitting window, the absorption is

191 significantly affected by the absorptions of NO_2 and O_3. To describe these two

192 absorption materials, temperature dependent cross section information are adopted. The

193 temperature dependent cross section setting considers the stratosphere and troposphere,

194 simultaneously.

195

196 **Table 2.** Ratio between SCD error and the SCD of O_2-O_2 according to the polynomial

197 order and offset settings used for DOAS fitting.

Polynomial	Offset = none	Offset = 0th
2nd order	6.06 ± 2.07	6.79 ± 2.31
3rd order	6.32 ± 2.20	6.79 ± 2.32
4th order	7.86 ± 2.78	7.34 ± 2.85

198

199 To minimize the noise effect and improve fitting quality, the optimal settings for

200 fitting were also analyzed. Table 2 shows ratios of SCD error to the SCD for various

201 polynomial and bias orders from observed radiance. The polynomial and offset are basic

202 fitting parameters for the DOAS fitting. Both two parameters describe the broadband

203 spectral feature of radiance. The ratio between SCD error and the SCD of O_2-O_2 is

204 important to determine the AEH retrieval quality. When the fitting error increase, the

205 uncertainty of AEH is also enhanced during the retrieval. Although the fitting quality

206 was good overall, the setting with 2nd order of polynomial and none offset was used for

207   the O_2-O_2 SCD estimation from the GEMS radiance due to the smallest fitting error.

208   After the estimation of O_2-O_2 SCD, conversion from O_2-O_2 SCD to AEH is an

209   essential process. For this conversion, a look-up table (LUT) approach between O_2-O_2

210   SCD and AEH was used with consideration of observation geometries, surface

211   conditions, and aerosol optical properties. Table 3 shows the dimension of the LUT for

212   the AEH retrieval algorithm. To calculate the LUT, a linearized pseudo-spherical vector

213   discrete ordinate radiative transfer model (VLIDORT) version 2.6 was used (Spurr,

214   2013). During the radiative transfer model simulation, the SSA and AOD is assumed to

215   be 440 nm. Although the center of O_2-O_2 absorption is 477 nm, the spectral discrepancy

216   between model assumed wavelength and center wavelength of O_2-O_2 absorption is

217   assumed to be ignored in this study. After calculating spectral radiance with 0.1 nm

218   sampling, we performed the slit response function of GEMS and sampling specification

219   prior to the DOAS fitting. For O_2-O_2 absorption, the absorption cross section used for

220   the radiative transfer model calculation is considered the temperature dependent

221   absorption cross section (e.g., Park *et al.*, 2017).

222   O_2-O_2 SCD decreases with increasing AEH for all aerosol types and AOD (Park *et al.*,

223   2016). The O_2-O_2 SCD sensitivity is enhanced at high AOD and absorbing dominant

224   aerosol cases. In addition, the contrast of O_2-O_2 SCD is greater for absorbing dominant

225   aerosols than non-absorbing aerosols. During the radiance passing through the aerosol

226   layer, the absorbing dominant aerosol is more efficiently absorbed the radiance. For this

227   reason, the effective optical path length is significantly shorter for absorbing aerosols.

228   Based on the changes in sensitivity observed for optical path length, aerosol type (in

229   particular in terms of SSA) and AOD are considered as input parameters for AEH

230   retrieval.

  Table 3. The dimension of the LUT for the GEMS AEH retrieval algorithm used to

  estimate AEH from O_2-O_2 SCD. (SZA: solar zenith angle, VZA: viewing zenith angle,

  RAA: relative azimuth angle, SUR: surface reflectance).

Variable [unit]	No. of entries	Entries	
Spectral range [nm]	-	455~491 nm (0.1 nm interval)	
SZA [º]	7	0.01, 10, 20, 30, 40, 50, 60	
VZA [º]	7	0.01, 10, 20, 30, 40, 50, 60	
RAA [º]	10	0.01,20, 40, 60, 80, 100, 120, 140, 160, 180	
SUR	3	0.0, 0.05, 0.2	
AOD at 440 nm	9	0.04, 0.2, 0.5, 1.0, 1.5, 2.0, 2.5, 3.0, 5.0	
Refractive Index (Imaginary) at 440 nm	3×3	Absorbing (Real: 1.45)	0.000, 0.0074, 0.0314
		Dust (Real: 1.53)	0.0, 0.0030, 0.0080
		Non-Absorbing (Real: 1.41)	0.0, 0.0040, 0.0156
AEH [km]	12	0.0 (Extrapolate), 0.2, 0.5, 1.0, 1.5, 2.0, 2.5, 3.0, 3.5, 4.0, 5.0, 10.0 (Extrapolate)	
Terrain Height [km]	2	0.0, 2.0	

  3. Data

  3.1. TROPOMI

  The TROPOMI is a spectrometer to observe the radiance from UV to near IR

  onboard the Sentinel-5 Precursor (Sentinel-5P) satellite. The orbit for Sentinel-5P is a

  polar orbit with ascending node crossing the equator at 13:30 local time. The aerosol

  layer height product from TROPOMI (AER_LH) retrieves vertically localized aerosol

layers in free troposphere with cloud free condition by using the level 1b earth radiance

measurements from 758 to 770 nm (de Graaf *et al.*, 2022). The definition of ALH from

TROPOMI is the optical centroid layer height of the plume. Spectral fit estimation of

reflectance around the O_2-A band is based on a neural network for the forward model

calculation for simulated condition. After cloud masking to avoid the cloud affected

pixels, an optimal estimation method was used to retrieve the aerosol layer height

parameters for the inversion method from observation. During the radiance fitting, the

ALH and AOD are fitted parameters, but other aerosol parameters, such as SSA, layer

thickness, and scattering phase function, are assumed to be fixed values (Nanda et al.,

2020). The target requirement on the accuracy and precision is 0.5 km or 50 hPa, and

the threshold requirement is 1 km or 100 hPa (de Graaf et al., 2022). In this study, we

use version 2.0.0 of the TROPOMI offline level 2 AER_LH product with the spatial

resolution is 3.5 km × 7 km at nadir viewing geometry.

3.2. CALIOP

The CALIOP is a spaceborne lidar onboard the Cloud-Aerosol Lidar and Infrared

Pathfinder Satellite Observations (CALIPSO) to measure the vertical information of

aerosol and cloud with estimating the optical properties. The CALIOP has two different

wavelength channels (532 and 1064 nm) by using the Nd:YAG laser to generate the

signals (Winker et al., 2009). The orbit for CALIPSO is Sun synchronous orbit

constelled to the A-train with ascending node, and also crosses to the equator at 13:30

local time. For the vertical information, the resolution for vertical sampling is 30 m

below 8 km altitude, and 60 m from 8 to 20 km altitude, respectively. Although the pixel

data can retrieve with extremely high horizontal and vertical resolutions, the spatial

265 coverage is narrow. In this study, the data of Level 2 aerosol profile product (APro,

266 version 3.41) was used. Representative layer height parameters (ALH and AEH) are

267 directly estimated by using the vertical profile of aerosol extinction coefficient at 532

268 nm.

269

270 **4. Case studies**

271 Figure 3 shows retrieval results for AEH, AOD, and SSA from GEMS on March 29

272 over East Asia. Because the operational schedule is hourly during the daytime, the

273 GEMS retrieval results are shown at 1-hour intervals from 01:00 to 07:00 Universal

274 Time Coordinated (UTC). From Park et al. (2016), thin AOD pixels have large AEH

275 uncertainty due to weak aerosol scattering information. For this reason, only AEH

276 retrieval results with AOD greater than 0.3 are shown in this study. During this case

277 study, a Yellow dust plume was located along the coast of China and South Korea with

278 AOD at 443 nm of 0.8~1.2. Simultaneously, another plume was also present over the

279 northeastern Korean Peninsula with AOD of 1.0~2.0 at 443 nm. SSA at 443 nm was

280 0.90~0.93 for the plume over South Korea and 0.87~0.90 for the plume over the

281 northeastern Korean Peninsula. Although the AOD and SSA for these plumes are

282 differed significantly, the retrieved AEH results from these different plumes show

283 similar ranges. For both plumes, AEH shows around 1.0~2.0 km in this case.

284
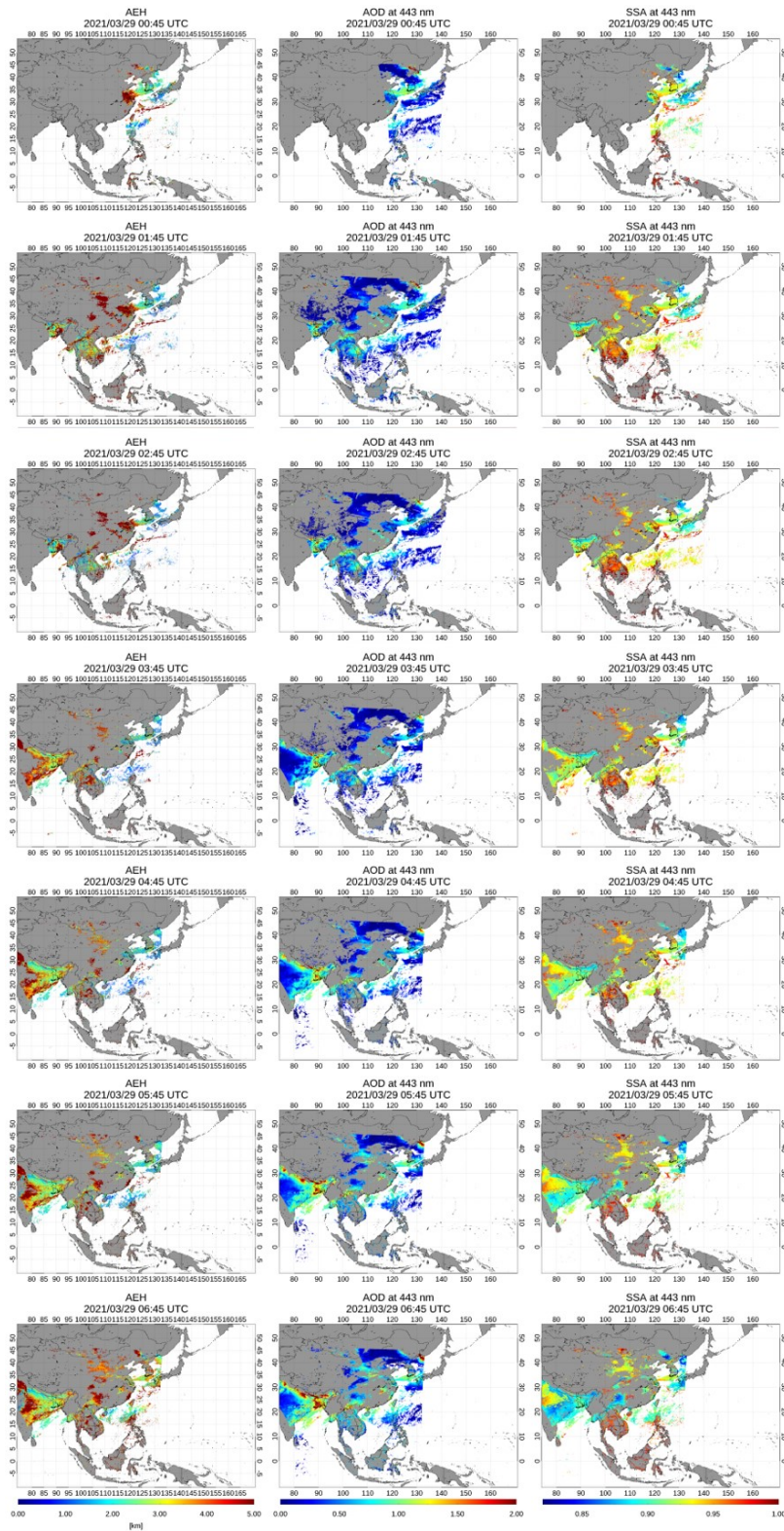
Figure 3. Case study results for AEH, AOD, and SSA based on GEMS observations

on March 29, 2021.

287   As shown in Figure 3, an additional severe aerosol plume was present over

288   northeastern India, with AOD at 443 nm of 1.0~2.0 and SSA at 443 nm of 0.85~0.90.

289   From Rana *et al.* (2019), metropolitan cities and industrial cluster in India are heavy

290   emitters of black carbon, and high concentrations of black carbon are distributed over

291   the Indo-Gangetic Plain (IGP). Therefore, the aerosol plume with high AOD and low

292   SSA (high absorbing) was a result that actually exists, and it was not a result with high

293   uncertainty due to edge of GEMS observation field. Except for the inland parts of India,

294   AEH in high AOD pixels ranged from 1.5 to 3.5 km.

295
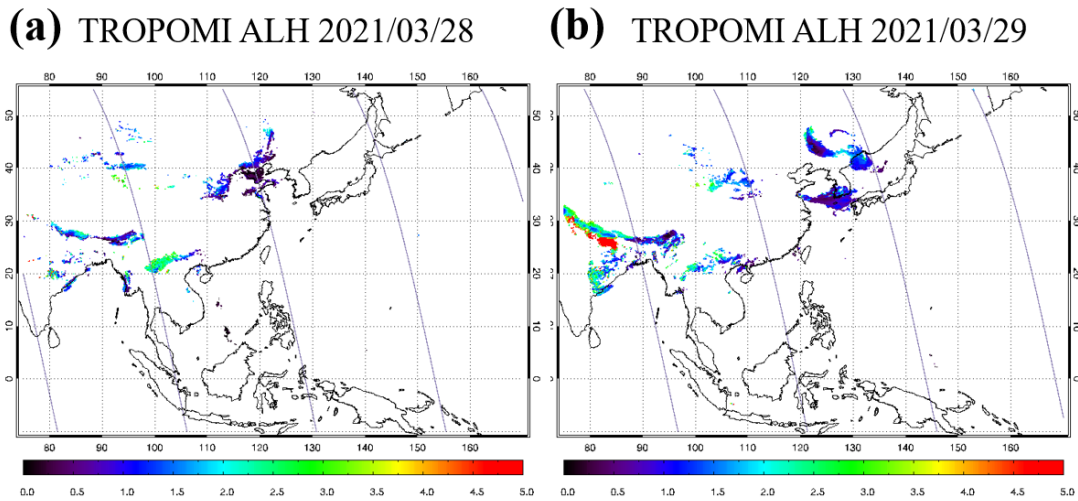
296   **Figure 4.** ALH retrieved from TROPOMI and orbit path of CALIOP on (a) March 28

297   and (b) March 29, 2021 (Unit: km).

298

299   For comparison of the retrieval, Figure 4 shows the ALH retrieved from TROPOMI

300   on March 28 and 29, 2021 over East Asia. A dust plume was transported from China to

301   South Korea during this period, then split into two distinct plumes over northeastern

302   China and the coastal area of South Korea. The ALH retrieved from TROPOMI for both

303   plumes were 0.5~1.5 km. Given the difference in definition for the aerosol height

304   parameters between ALH and AEH, relatively high height values were retrieved from

305   GEMS compared to TROPOMI. In an ideal case under symmetric gaussian distribution

306   with a width of 1 km, the AEH from GEMS was around 0.5 km higher than the peak

307   height of aerosol layer. The ALH expresses the center (or peak) height, thus, the AEH

308   from GEMS was overestimated by around 0.5 km relative to the ALH from TROPOMI.

309   Although AEH had higher values than ALH from TROPOMI, the GEMS AEH

310   retrievals for the dust transport case study were successfully retrieved and mostly shown

311   the expected uncertainty of 1 km.

312   Furthermore, the AEH retrieved pixels covered by GEMS is larger than by

313   TROPOMI, as demonstrated by a comparison of Figures 3 and 4. In East Asia, AEH

314   from GEMS estimated a continuous dust plume from China to South Korea. In addition,

315   the GEMS retrieval more widely estimated aerosol height information in coastal India

316   compared to TROPOMI. Although high AEH values were retrieved for low AOD

317   regions over low latitude ocean surface, the AEH from GEMS was successfully

318   retrieved over the area of interest for the case study.

319

320
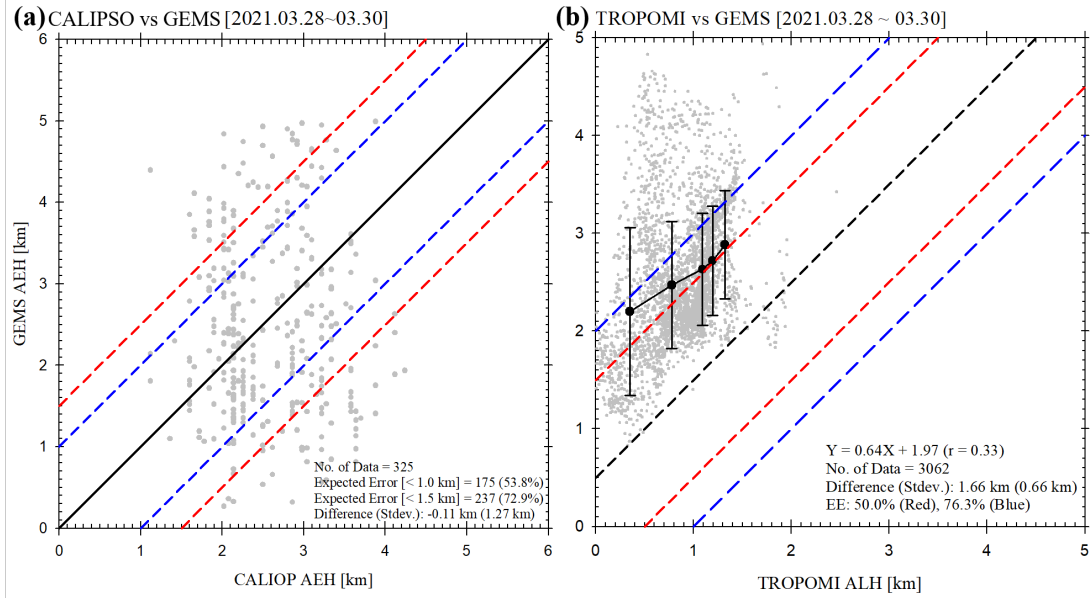
Figure 5. Intercomparison of (a) AEH between CALIOP and GEMS and (b) ALH from TROPOMI and AEH from GEMS (black dot and error bar is mean and standard deviation in 20% interval of each TROPOMI ALH) over the period from March 28 to 30, 2021.

Figure 5 shows intercomparison results for aerosol plume height among GEMS, CALIOP, and TROPOMI during the case study of Yellow dust transport in East Asia from March 28 to 30, 2021. For spatial colocation, we selected pixels for which distance between GEMS and CALIOP observations was less than 50 km. In addition, only the closest 10% of pixels were used. Given the different orbital characteristics of CALIOP and GEMS, temporal colocation was also considered. During the period of image scanning from east to west over Asia by GEMS, CALIOP passes through the GEMS observation area from south to north every 98.3 minutes. On average, CALIOP passes three to four orbits through the GEMS scan area during a single day of daytime observation. To consider these different orbital characteristics, temporal colocation was

336   limited to a 1-hour difference between CALIOP and GEMS scans. As GEMS observes

337   hourly, colocated pixels between the two satellites shift from east to west over time.

338   Ultimately, the number of colocated pixels with AOD at 443 nm > 0.3 was 534 for this

339   case study.

340   For the direct comparison shown in Figure 5a, the difference in AEH between GEMS

341   and CALIOP was -0.11±1.27 km. Nanda *et al.* (2020) reported that the difference in

342   ALH between TROPOMI and CALIOP was 0.53 km for 4 cases of thick Saharan dust

343   plumes. In addition, 53.8% and 72.9% of the total pixels showed differences less than

344   1.0 and 1.5 km, respectively. Large AEH uncertainty occurred mostly over the inland

345   area of China. Because AEH from GEMS uses only the O_2-O_2 absorption band, the

346   accuracy of AEH is sensitive to uncertainty in surface reflectance and AOD. Recently,

347   GEMS accurately estimated surface reflectance in near real time in operation. However,

348   this study used the minimum reflectance under the Lambertian assumption to retrieve

349   AOD and AEH to coincide with the use of surface information on L2AERAOD and

350   AEH retrieval.

351
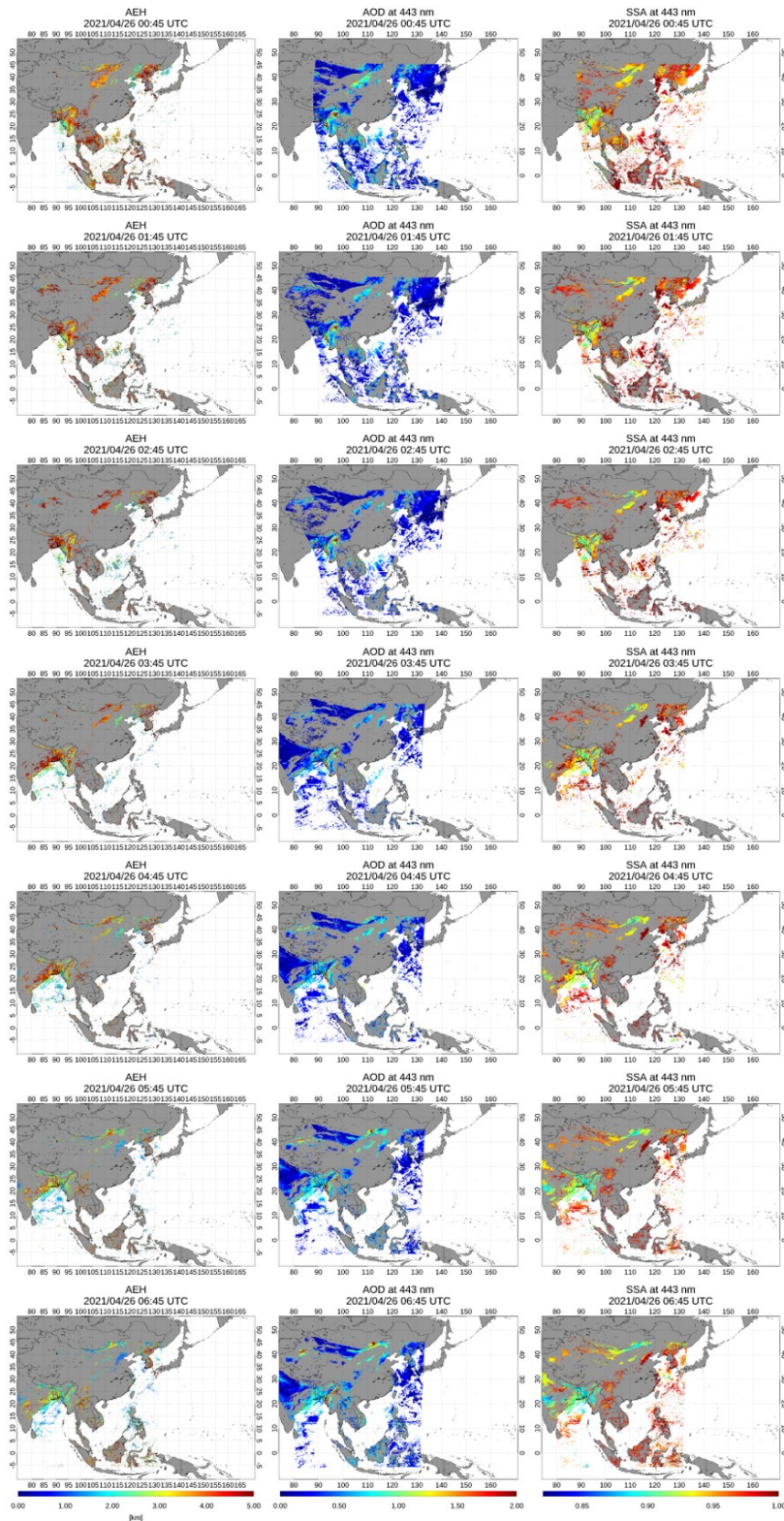
Figure 6. Case study results for AEH, AOD, and SSA based on GEMS observations

on April 26, 2021.

354   Figure 5b shows a comparison of GEMS and TROPOMI for the period of March 28

355   ~ 30, 2021 in East Asia. To ensure the accuracy of ALH from TROPOMI, only pixels

356   with quality assurance (QA) values greater than 0.5 were used. The difference between

357   GEMS AEH and TROPOMI ALH was 1.66 ± 0.66 km in this case, and 49.9% of all

358   pixels had differences less than 1.5 km. This proportion value was lower than the

359   corresponding result from the comparison of GEMS and CALIOP. However, the ALH

360   from TROPOMI is generally lower than the AEH from GEMS because of the

361   discrepancy in definitions. To correct the inconsistency of definition between ALH and

362   AEH, the difference between two retrieval results decreased to 0.5 km bias. After

363   correction, 50.0% and 76.3% of pixels are within the expected error ranges of 1.0 and

364   1.5 km, respectively.

365
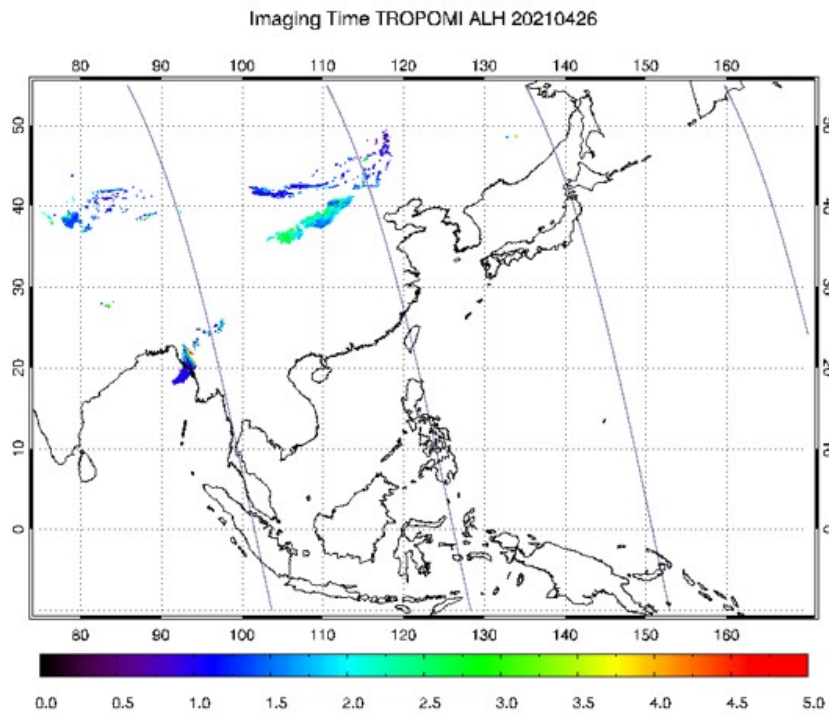
366   **Figure 7.** ALH retrieved from TROPOMI and orbit path of CALIOP on April 26,

367   2021 (Unit: km).
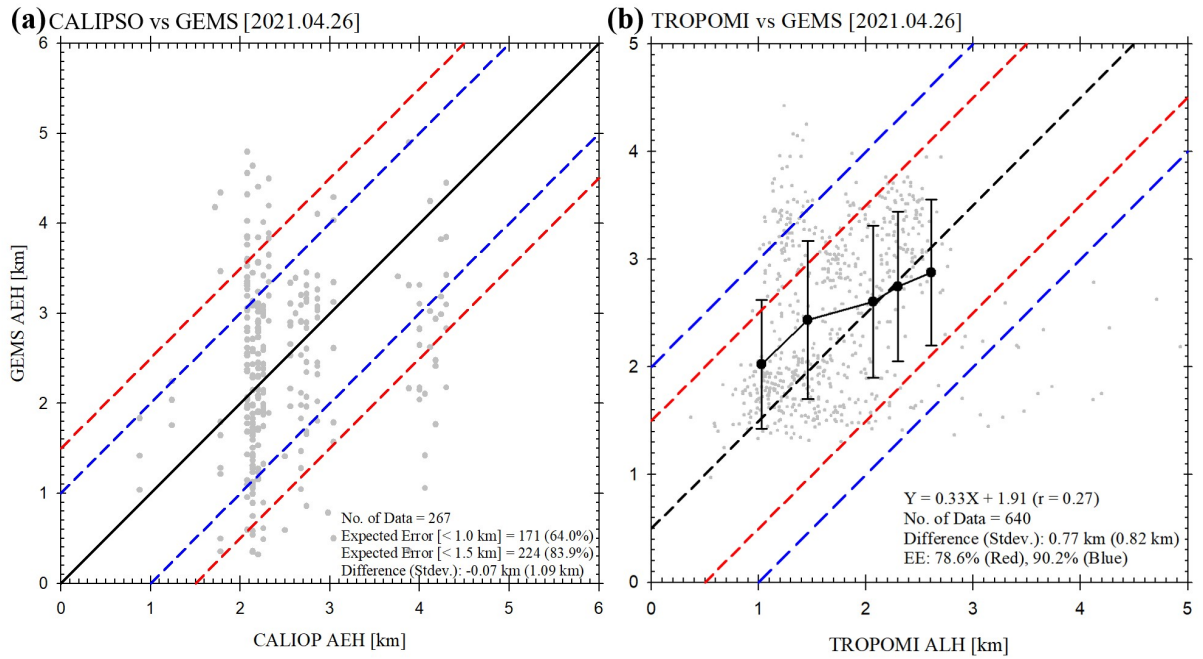
Figure 8. Intercomparison of (a) AEH between CALIOP and GEMS, and (b) ALH from

TROPOMI and AEH from GEMS (black dot and error bar is mean and standard

deviation in 20% interval of each TROPOMI ALH) on April 26, 2021.

An additional intercomparison case of April 26, 2021 is shown in Figures 6 (GEMS)

and 7 (TROPOMI). During the transport of the Yellow dust plume from inland China to

the coastal area, AEH changed from 4.0 km at 02:00 UTC to 2.0 km at 06:00 UTC. By

contrast, ALH from TROPOMI only observed the 1.5~2.5 km layer height over East

Asia around 04:00 UTC. Although the AEH from GEMS had spatio-temporal

uncertainty, this case demonstrates the advantage of AEH retrieval from GEMS for

continuous monitoring of changes in plume height, in particular during dust transport.

As shown in Figure 8, AEH from GEMS showed differences in height of -0.07 ± 1.09

km (compared to CALIOP) and 0.77 ± 0.82 km (compared to TROPOMI).

5. Long-term validation

For long-term validation, we used the AEH retrieval results from January to June, 2021. Similar to the case studies, intercomparison datasets from CALIOP and TROPOMI were selected containing mean layer height values in the closest 10% of pixels within a 50 km range for spatial colocation. In addition, only observations taken within ±1 hour of the GEMS observation time were selected for temporal colocation. As the CALIOP and TROPOMI satellites passed over the study area around 13:30 local time, which is around 04:30 UTC for East Asia and around 06:30 UTC for India. Most temporal colocation pixels aligned with observation times of 04:00~06:00 UTC, respectively. To check the dependence of several retrieval variables, the AI value for UV (UVAI), AOD, SSA, and dominant aerosol type in each pixel (TYPE) were obtained from the L2AERAOD. Although the GEMS algorithm retrieved AEH in the range of 0~10 km, the sensitivity of O_2-O_2 SCD was weak in cases of high AEH because of the vertical distribution of air molecules. To ensure sufficient quality of retrieved data, therefore, the AEHs from GEMS and CALIOP, and the ALH from TROPOMI were used only in pixels where the AEH from GEMS were lower than 5 km.
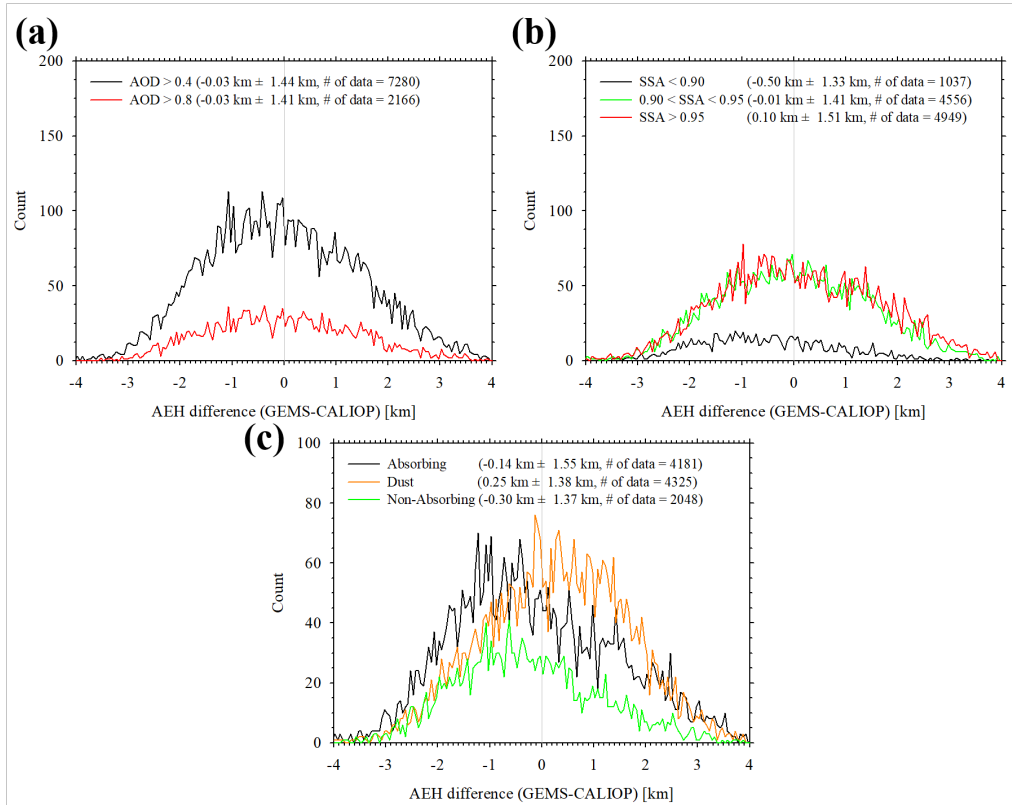
Figure 9. Histogram of AEH difference between CALIOP and GEMS with respect to (a) AOD, (b) SSA, and (c) TYPE from GEMS over the period from January 1 to June 30, 2021.

Figure 9 shows histograms of difference in AEH between GEMS and CALIOP according to AOD at 443 nm, SSA at 443 nm, and TYPE from GEMS. From Figure 9a, the dependence on AOD threshold was insignificant; the average estimated AEH difference was -0.03 km, but the variation in AEH difference was around 1.4 km based on the standard deviation for AOD > 0.4. Because of uncertainty in GEMS operational products, AEH from GEMS exhibits large variability. Although L2AERAOD from GEMS retrieved the AOD, SSA, and aerosol types, the retrieved results from L2AERAOD include significant uncertainty. Go *et al.* (2020) noted that the UV aerosol

retrieval algorithm, which is the basic method to the L2AERAOD algorithm, has significant discrepancies for both AOD and SSA compared to ground-based data. In addition, significant fitting error perturbs the fitting signals and tends to result in the underestimation of SCD. Although the fitting error of O_2-O_2 SCD from GEMS radiance was minimized, the fitting error is still remained around 6%, as indicated in Table 2. The discrepancy in fitting condition between the simulated and observed radiance biased the SCD estimation, which in turn led to bias and variation in the AEH retrieval. Combined with the high sensitivity of AEH errors to aerosol optical properties, uncertainty arising from L2AERAOD causes significant variability in AEH.

The variation in AEH difference between observation platforms is shown in Figure 9b as a histogram according to SSA threshold. Across the entire SSA threshold range, the standard deviation of the AEH difference was 1.33~1.51 km. In particular, this standard deviation decreased slightly with decreasing SSA. Aerosol height information is significantly more sensitive to absorbing-dominant aerosols than scattering-dominant aerosols (e.g., Park *et al.*, 2016; Nanda *et al.*, 2020). Even if the uncertainty due to aerosol properties is fixed, the variability of AEH is affected by the sensitivity of AEH error to aerosol absorptivity.

Figure 9c shows the dependence of AEH difference on TYPE. Changing the Type significantly changed the mean value of AEH difference. The TYPE product included dependence on the aerosol size and optical absorptivity. For this reason, the AEH difference graphs for the "Dust" and "Absorbing" types differ, despite both types being absorbing-dominant aerosols. The AEH difference for the "Absorbing" type showed a negative bias with a large standard deviation, whereas a positive bias with a small standard deviation was obtained for the "Dust" type. The AEH difference for the "Non-

Absorbing" aerosol type showed the largest negative bias in this comparison. These

results suggest that the aerosol size distribution of fine particles affects the negative bias

of AEH. Combined with the AEH difference bias illustrated in Figure 8b, these findings

indicate that the bias in AEH difference for "Absorbing" aerosols is weakened by their

absorbing-dominant property.

Figure 10 shows means and standard deviations for AEH difference between

CALIOP and GEMS according to AOD and AI values from GEMS. For AOD, the mean

AEH difference ranged from -0.13 to 0.03 km with a standard deviation of

approximately 1.45 km. Similar to Figure 9a, the variation in AEH difference with AOD

change was insignificant. For AI, the smallest AEH difference was -0.19 km, obtained

for the AI range of 1.5~2.0. The largest AEH difference was 0.24 km for the AI range of

4.0~4.5. Although the AEH difference varied slightly, no consistent tendency in AEH

variation with AI was observed Overall, the standard deviation of AEH difference

ranged from 1.49 km ($0.0 < AI < 0.5$) to 1.18 km ($4.5 < AI < 5.0$), and a consistent

tendency of decreasing variance in AEH difference was found with increasing AI.

451
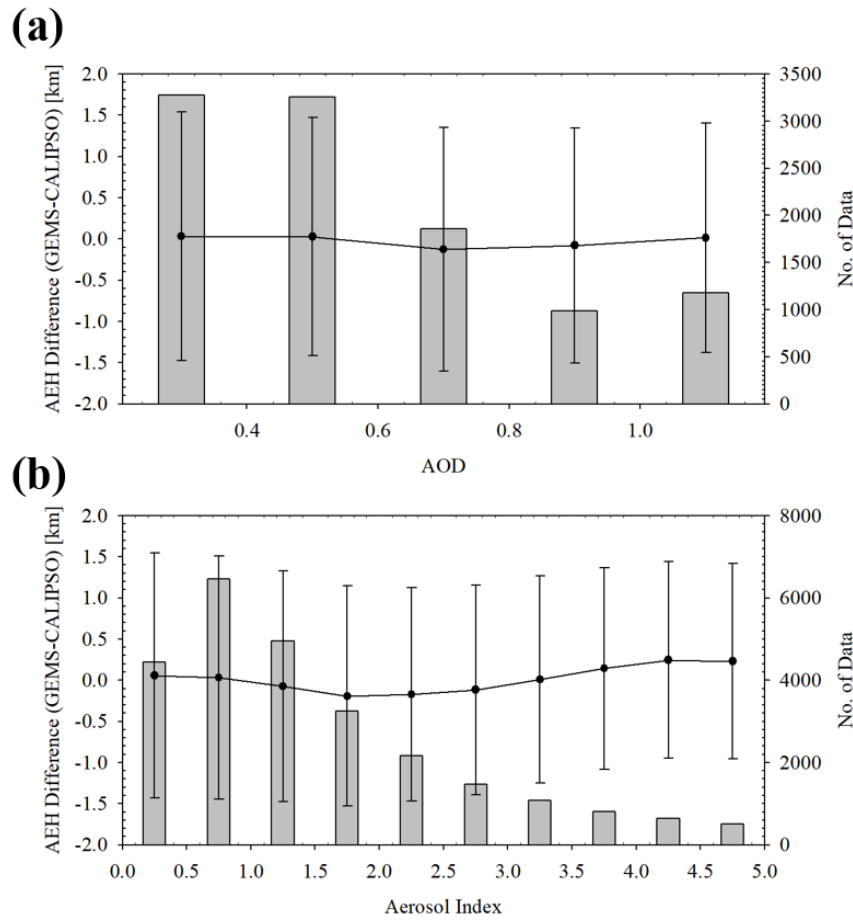
Figure 10. AEH difference between CALIOP and GEMS with respect to ranges of (a)

AOD and (b) AI obtained from GEMS from January 1 to June 30, 2021 (line and error

bar is the mean and standard deviation of AEH difference, and the box is number of

data).

Figure 11 shows histograms of differences between ALH from TROPOMI and AEH

from GEMS [(AEH from GEMS) – (ALH from TROPOMI)] according to the SSA and

TYPE obtained from GEMS. As TROPOMI retrieved only ALH data with high QA

values over pixels containing strong aerosol plumes, the AOD dependence of aerosol

height difference is not shown in this comparison. In addition, the number of pixels

462   corresponding to non-absorbing aerosols (i.e., pixels with SSA > 0.95 or "Non-

463   Absorbing" type) was insufficient. Nanda *et al.* (2020) showed that the operational

464   algorithm of TROPOMI is only retrieved the ALH over absorbing dominant aerosol

465   pixels. In addition, Griffin *et al.* (2020) reported that the pixels with small positive

466   UVAI (weak absorbing cases) pixels are identified with small QA values in the offline

467   product of ALH.
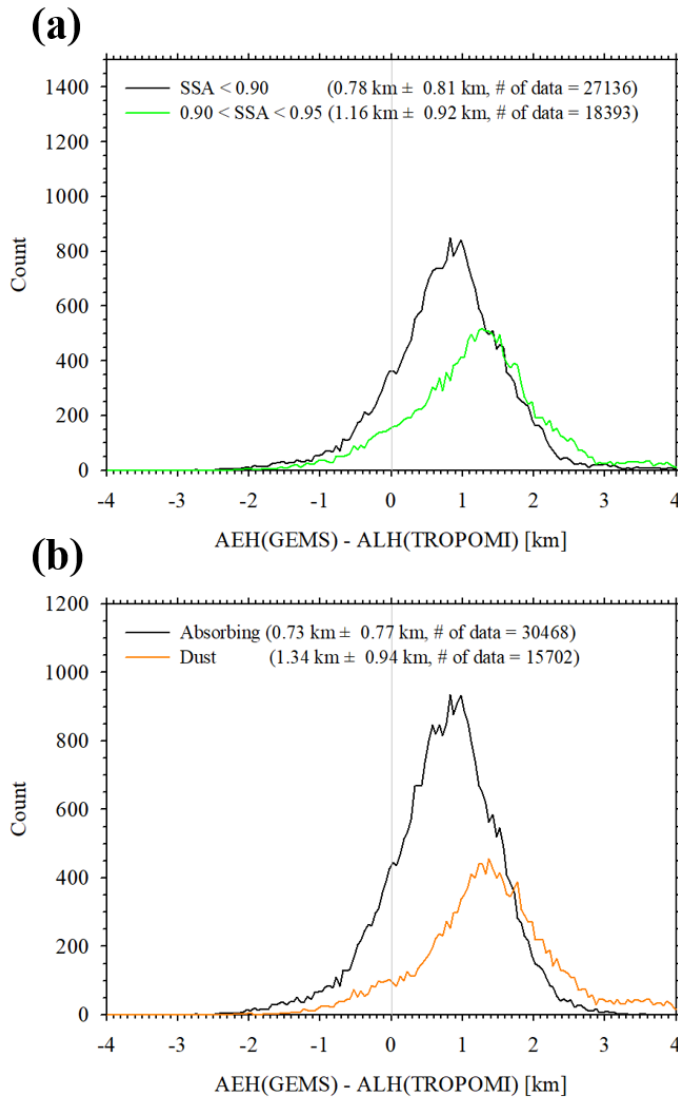
468

469   **Figure 11.** Histograms of differences between ALH from TROPOMI and AEH from

470   GEMS [(AEH from GEMS) – (ALH from TROPOMI)] with respect to (a) SSA, and (b)

471 TYPE from GEMS in the period from January 1 to June 30, 2021.

472   As shown in Figure 11, (AEH from GEMS) − (ALH from TROPOMI) was

473 significantly dependent on both SSA and TYPE. The mean value of (AEH from GEMS)

474 − (ALH from TROPOMI) decreased as the aerosol absorptivity increased. This

475 difference was 0.78 ± 0.81 and 1.16 ± 0.92 km for pixels of SSA < 0.90 and 0.90 < SSA

476 < 0.95, respectively. Comparing these results to Figure 8b, we find that the standard

477 deviation of the comparison with TROPOMI was approximately 60% of the

478 corresponding value for CALIOP. It is because both TROPOMI and GEMS are passive

479 sensors that use similar retrieval methods for oxygen absorption bands.

480   In addition, (AEH from GEMS) − (ALH from TROPOMI) was significantly

481 dependent on TYPE, as shown in Figure 10b. The difference was 0.73 ± 0.77 and $1.34 \pm$

482 0.94 km for "Absorbing" and "Dust" type aerosols, respectively. Similar to Figure 8c,

483 the TYPE dependence of aerosol height information was influenced by both

484 absorptivity and size information. In addition, the difference in the definition of ALH

485 from TROPOMI and AEH from GEMS impacted the comparison. "Dust" types of

486 aerosol are mainly transported in the free troposphere, and the associated plume

487 thickness is highly variable. By contrast, "Absorbing" aerosols mainly originate from

488 anthropogenic emissions in East Asia (e.g., Gao *et al.*, 2014; Wang *et al.*, 2012; Peng *et*

489 *al.*, 2016). In addition, the vertical distribution of aerosols is unstable for "Dust" case.

490 For these reasons, the standard deviation of aerosol height was larger for the "Dust"

491 type.

492
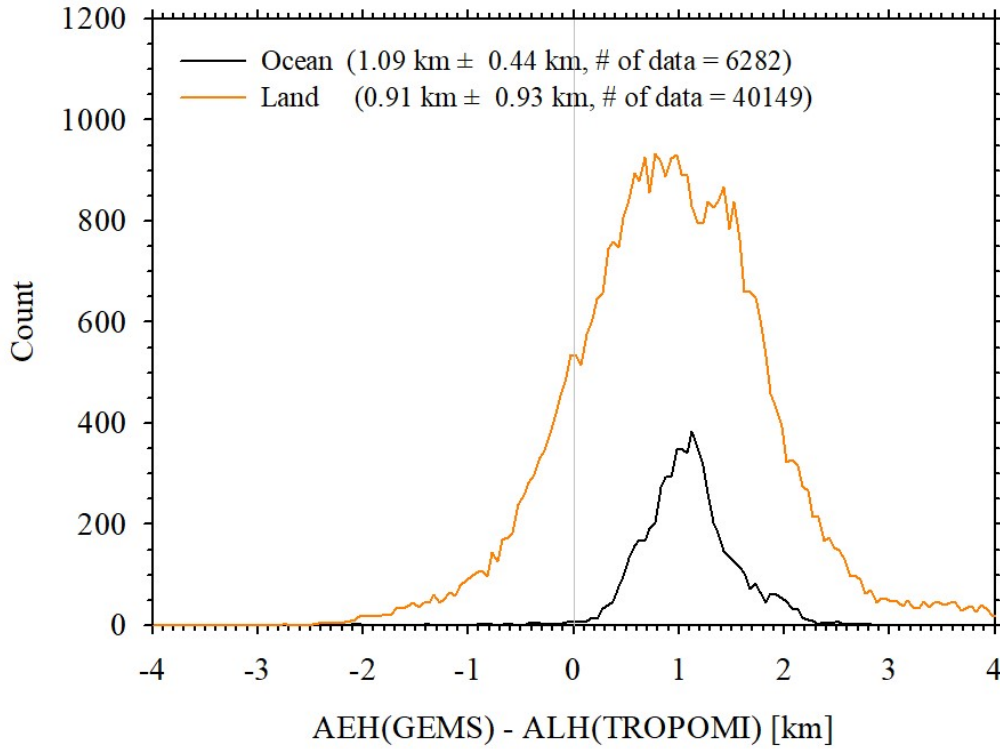
Figure 12. Histogram of the difference between ALH from TROPOMI and AEH from GEMS [(AEH from GEMS) – (ALH from TROPOMI)] over land and ocean pixels, respectively, from January 1 to June 30, 2021.

496

The non-Lambertian effect on the land surface impacted surface albedo uncertainty during AEH retrieval, and this effect led to bias and variance in AEH. In this study, the minimum Lambertian equivalent reflectance was used as the reference reflectance value. However, surface reflectivity has geometric dependence due to non-Lambertian effects, which leads to a bias of 0.01-0.02 for surface reflectance over the land surface (e.g., Qin *et al.*, 2019). To identify the sensitivity of surface property, a histogram was constructed of (AEH from GEMS) – (ALH from TROPOMI) after classification into land and ocean surface types, as shown in Figure 12. From the statistical results, the mean differences

505   were estimated to be 1.09 and 0.91 km for ocean and land pixels, respectively,

506   indicating insignificant difference in bias between these two surface covers. However,

507   the standard deviation of the two surface types indicated a significant difference. Over

508   the ocean surface, the histogram is very narrow. Although there are 6.5 times more data

509   for land than those for the ocean surface, the land surface has a relatively wide

510   histogram distribution. This discrepancy arises because the non-Lambertian effect

511   causes bias in surface reflectance, while also influencing the variability in surface

512   reflectance related to observation geometry. For this reason, land surface reflectance

513   based on the non-Lambertian surface assumption is not fully representative of actual

514   surface reflectance as a function of observation geometry. Therefore, the standard

515   deviation of the layer height difference is larger over the land surface, and the

516   significant difference between land and ocean pixels is mainly driven by the assumption

517   of surface reflection properties.
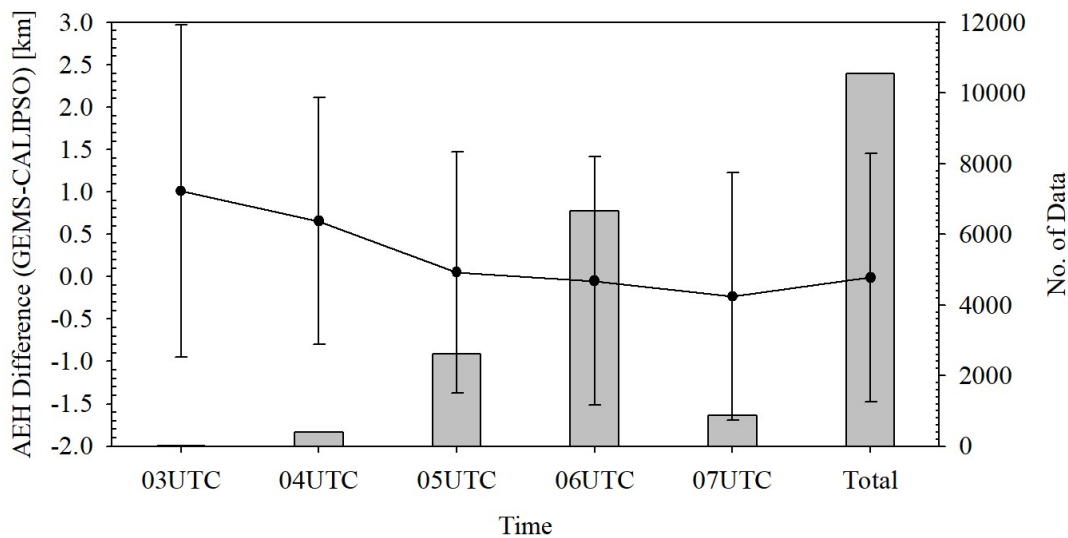
519   **Figure 13.** Diurnal dependence of AEH difference between CALIOP and GEMS

520   from January 1 to June 30, 2021 (line and error bar is the mean and standard deviation

521 of AEH difference, and the box is number of data).

522   The results of hourly statistical analyses are presented in Figure 13. Because they use

523 a consistent definition of AEH, we show only a comparison of GEMS and CALIOP. The

524 diurnal variation in AEH difference ranged from -0.23 ± 1.45 km (07:00 UTC, Number

525 of Data = 867) to 1.01 ± 1.96 km (03:00 UTC, Number of Data = 23). However, the

526 number of pixels observed at 03:00 UTC was insufficient for the identification of

527 diurnal variation. The AEH difference of 0.66 ± 1.45 km was the next highest value

528 obtained at 04:00 UTC (Number of Data = 395). The inhomogeneous number of data is

529 mainly due to the lack of spatial homogeneity among retrieval pixels. Over India, very

530 high AOD values were consistently observed during the comparison period. Otherwise,

531 the AEH was only retrieved under conditions of severe anthropogenic emissions over

532 East Asia. In addition, the diurnal variation in AEH difference was caused by spatial

533 characteristics of AEH difference. From 03:00 to 05:00 UTC, CALIOP mainly passed

534 over East Asia, which has numerous sources of aerosol emissions, including biomass

535 burning, dust, and industrial activity. In addition, GEMS observed only the eastern part

536 of India, which is dominated by anthropogenic aerosols. The spatial distribution of the

537 dominant aerosol types may impact the diurnal variation in AEH difference.

538

539 **6. Summary & Conclusions**

540   Based on the possibility of retrieving AEH from environmental satellite sensors, an

541 AEH retrieval algorithm for GEMS was developed that solely uses the O_2-O_2 absorption

542 band with considering aerosol and surface properties. Because the sensitivity of AEH

543 retrieval is strongly affected by optical amounts and properties of aerosols, as well as

544 surface reflectivity, an AEH retrieval algorithm for GEMS was developed after retrieval

545 of the GEMS operational algorithms, L2AERAOD and L2SFC. With the newly

546 developed retrieval algorithm, GEMS can be used to monitor aerosol vertical

547 information with high temporal and spatial resolution. To ensure significant sensitivity

548 of AEH retrieval, only AEH retrieval results are with AOD larger than 0.3 were shown.

549 For dust plumes over East Asia, AEH indicated significant aerosol vertical

550 information and insignificant diurnal variation in regions with severe dust plumes. After

551 spatial and temporal colocation, the AEH from GEMS aligned well with the AEH

552 information obtained from CALIOP. The differences in AEH between GEMS and

553 CALIOP for dust plume cases were -0.07 ± 1.09 and -0.11 ± 1.27 km, with 53.8% and

554 72.9% of all pixels showing differences less than 1.0 and 1.5 km, respectively. Large

555 AEH uncertainty was found mostly over inland China due to uncertainty in surface

556 reflectance and AOD over the land surface. In addition, AEH from GEMS was

557 overestimated compared to the TROPOMI ALH results due to different definitions of

558 ALH from TROPOMI and AEH from GEMS.

559 In long-term intercomparison with CALIOP, the average AEH difference was

560 estimated to be -0.03 km, with variation of around 1.4 km based on the standard

561 deviation for AOD > 0.4. In terms of sensitivity to surface albedo, the mean differences

562 were estimated to be 1.09 and 0.91 km over the ocean and land, respectively, which is

563 an insignificant difference of the biases between these two surface types. The large

564 variation in AEH difference between GEMS and CALIOP was caused by uncertainty in

565 the input parameters estimated from L2AERAOD and L2SFC. In the long-term

566 intercomparison with TROPOMI, this difference was significantly dependent on both

567 SSA and TYPE. The difference was 0.78 ± 0.81 km and 1.16 ± 0.92 km for pixels with

568 SSA < 0.90 and 0.90 < SSA < 0.95, respectively. In addition, differences of 0.73 ± 0.77

and 1.34 ± 0.94 km were obtained for the "Absorbing" and the "Dust" types of aerosol, respectively. The AEH difference ranged from -0.23 ± 1.45 km (07:00 UTC, Number of Data = 867) to 1.01 ± 1.96 km (03:00 UTC, Number of Data = 23), showing diurnal dependence. The spatial difference in dominant aerosol type may impact the diurnal variation in AEH difference.

The case studies and results of the long-term validation show that AEH retrieved from GEMS can provide information on aerosol vertical distribution, with applications in diverse research fields. In particular, AEH information can be applied to AMF calculation for trace gases to consider the change in scattering weight change due to the presence of an aerosol layer. In addition, AEH considerably affects the surface particulate matter (PM) concentration obtained from satellite-based AOD because PM estimation is significantly affected by the mixing layer height of aerosols.

Although several fields of study may apply the AEH retrieval results, retrieval uncertainty in AEH remains due to the uncertainty of retrieved AOD and SSA. In addition, the uncertainty in surface reflectance and the discrepancy in O_2-O_2 SCD values between the simulation results and observations can be affected to the potential error sources of AEH from GEMS. Moreover, AEH provides representative layer height information as only one variable because of its sole reliance on O_2-O_2 SCD for direct estimation of aerosol height information. This method is limited to the consideration of aerosol vertical structures (i.e., Gaussian or exponential vertical distribution structures). Rather than using the GEMS sensor alone, using another absorption band for oxygen-based materials would provide additional scattering information about aerosols.

592 **Acknowledgements**

593   This work was supported by the National Institute of Environment Research of the

594 Republic of Korea under Grant NIER-2023-04-02-050.

595

References

Accarreta, J. R., de Haan, J. F., and Stammes, P.: Cloud pressure retrieval using the O2-O2 absorption band at 477 nm, J. Geophys. Res., 109, D05204, doi:10.1029/2003JD003915, 2004

Ahn, C., Torres, O., and Jethva, H.: Assessment of OMI near-UV aerosol optical depth over land, J. Geophys. Res., 119, 2457-2473, 2014.

Bogumil, K., Orphal, J., Burrows, J. P., and Flaud, J. M.: Vibrational progressions in the visible and near-ultraviolet absorption spectrum of ozone, Chem. Phys. Lett., 349, 241-248, 2001.

Buchard, V., de Silva, A. M., Colarco, P. R., Darmenov, A., Randles, C. A., Govindaraju, R., Torres, O., Campbell, J., and Spurr, R.: Using the OMI aerosol index and absorption aerosol optical depth to evaluate the NASA MERRA Aerosol reanalysis, Atmos. Chem. Phys., 15, 5743-5760, 2015.

Chen, X., Wang, J., Xu, X., Zhou, M., Zhang, H., Garcia, L. C., Colarco, P. R., Janz, S. J., Yorks, J., McGill, M., Reid, J. S., de Graaf, M., and Kondragunta, S.: First retrieval of absorbing aerosol height over dark target using TROPOMI oxygen B band: Algorithm development and application for surface particulate matter estimates, Remote Sens. Env., 265, 112674, 2021.

Chimot, J., Veefkind, J. P., Vlemmix, T., de Haan, J. F., Amiridis, V., Proestakis, E., Marinou, E., and Levelt, P. F.: An exploratory study on the aerosol height retrieval from OMI measurements of the 477 nm O2-O2 spectral band using a neural network approach, Atmos. Meas. Tech., 10, 783-809, 2017.

Choi, H., Liu, X., Abad, G. G., Seo, J., Lee, K. -M., and Kim, J.: A fast retrieval of cloud parameters using a Triplet of wavelengths of oxygen dimer band around 477 nm, Remote Sens., 13, 152, doi: 10.3390/rs13010152, 2021.

Choi, W., Lee, H., Kim, J., Ryu, J. -Y., Park, S. S., Park, J., and Kang, H.: Effects of spatiotemporal O4 column densities and temperature-dependent O4 absorption cross-section on an aerosol effective height retrieval algorithm using the O4 air mass factor from the ozone monitoring instrument, Remote Sens. Env., 229, 223-233, 2019.

626 Choi, W., Lee, H., and Kim, J.: First TROPOMI retrieval of aerosol effective height
627   using O4 absorption band at 477 nm and aerosol classification, IEEE Trans.
628   Geosci., Remote Sens., 59, 9873-9886, 2021.

629 de Graaf, M., Stammes, P., Torres, O., and Koelemeijer, R. B. A.: Absorbing aerosol
630   index: Sensitivity analysis, application to GOME and comparison with TOMS, J.
631   Geophys. Res., 110, D01201, doi:10.1029/2004JD005178, 2005.

632 de Graaf, M., de Haan, J. F., and Sanders, A. F. J.: TROPOMI ATBD of the Aerosol
633   Layer Height, 75pp, Royal Netherlands Meteorological Institute, Netherland.

634 Ding, S., Wang, J., and Xu, X.: Polarimetric remote sensing in oxygen A and B bands:
635   Sensitivity study and information content analysis for vertical profile of aerosols,
636   Atmos. Meas. Tech, 9, 2077-2092, 2016.

637 Dubuisson, P., Frouin, R., Dessaily, D., Duforet, L., Leon, J. –F., Voss, K., and Antoine,
638   D.: Estimating the altitude of aerosol plumes over the ocean from reflectance ratio
639   measurements in the O2 A-band, Remote Sens. Environ., 113, 1899-1911,
640   doi:10.1016/j.rse.2009.04.018, 2009.

641 Gao, Y., Zhao, C., Liu, X., Zhang, M., and Leung, L. R.: WRF-Chem simulations of
642   aerosols and anthropogenic aerosol radiative forcing in East Asia, Atmos. Environ.,
643   92, 250-266, 2014.

644 Geddes, A., and Boesch, H.: Tropospheric aerosol profile information from high-
645   resolution oxygen A-band measurements from space, Atmos. Meas. Tech., 8, 859-
646   874, 2015.

647 Go, S., Kim, J., Park, S. S., Kim, M., Lim, H., Kim, J. -Y., Lee, D. -W., and Im, J.:
648   Synergistic use of hyperspectral UV-visible OMI and broadband meteorological
649   imager MODIS data for a merged aerosol product, Remote Sens., 12, 3987,
650   doi:10.3390/rs12233987, 2020.

651 Griffin, D., Sioris, C., Chen, J., Dickson, N., Kovachik, A., de Graaf, M., Nanda, S.,
652   Veefkind, P., Dammers, E., McLinden, C. A., Makar, P., and Akingunola, A.: The
653   2018 fire season in North America as seen by TROPOMI: aerosol layer height
654   intercomparisons and evaluation of model-derived plume heights, Atmos. Meas.
655   Tech., 13, 1427-1445, 2020.

656   Herman, J. R., Bhartia, P. K., Torres, O., Hsu, C., Seftor, C., and Celarier, E.: Global
657   distribution of UV-absorbing aerosols from Nimbus-7/TOMS data, J. Geophys.
658   Res., 102(D14), 16911-16922, 1997.

659   Hong, H., Lee, H., Kim, J., Jeong, U., Ryu, J., and Lee, D. S.: Investigation of
660   simultaneous effects of aerosol properties and aerosol peak height on the air mass
661   factors for space-borne NO2 retrievals, Remote Sens., 9, 208,
662   doi:10.3390/rs9030208, 2017.

663   Joiner, J., and Bhartia, P. K.: The determination of cloud pressures from rotational
664   Raman scattering in satellite backscatter ultraviolet measurements, J. Geophys.
665   Res., 100, 23019-23026, 1995.

666   Joiner, J., and Vasilkov, A. P.: First results from the OMI rotational Raman scattering
667   cloud pressure algorithm, IEEE Trans. Geosci. Remote Sens., 44, 1272-1282, 2006.

668   Kim, M., Kim, J., Torres, O., Ahn, C., Kim, W., Jeong, U., Go, S., Liu, X., Moon, K. J.,
669   and Kim D. -R.: Optimal estimation-based algorithm to retrieve aerosol optical
670   properties for GEMS measurements over Asia, 10, 162, doi:10.3390/rs10020162,
671   2018.

672   Kim, J., Jeong, U., Ahn, M. -H., Kim, J. H., Park, R. J., Lee, H., Song, C. H., Choi, Y. -
673   S., Lee, K. -H., Yoo, J. -M., Jeong, M. -J., Park, S. K., Lee, K. -M., Song, C. -K.,
674   Kim, S. -W., Kim, Y. J., Kim, S. -W., Kim, M., Go, S., Liu, X., Chance, K., Chan
675   Miller, C., Al-Saadi, J., Veihelmann, B., Bhartia, P. K., Torres, O., González Abad,
676   G., Haffner, D. P., Ko, D. H., Lee, S. H., Woo, J. -H., Chong, H., Park, S. S., Nicks,
677   D., Choi, W. J., Moon, K. -J., Cho, A., Yoon, J., Kim, S. -K., Hong, H., Lee, K.,
678   Lee, H., Lee, S., Choi, M., Veefkind, P., Levelt, P. F., Edwards, D. P., Kang, M., Eo,
679   M., Bak, J., Baek, K., Kwon, H. -A., Yang, J., Park, J., Han, K. M., Kim, B. -R.,
680   Shin, H. -W., Choi, H., Lee, E., Chong, J., Cha, Y., Koo, J. -H., Irie, H., Hayashida,
681   S., Kasai, Y., Kanaya, Y., Liu, C., Lin, J., Crawford, J. H., Carmichael, G. R.,
682   Newchurch, M. J., Lefer, B. L., Herman, J. R., Swap, R. J., Lau, A. K. H., Kurosu,
683   T. P., Jaross, G., Ahlers, B., Dobber, M., McElroy, C. T., and Choi, Y.: New era of
684   air quality from Space: Geostationary Environment Monitoring Spectrometer
685   (GEMS), Bul. Ame. Meteorol. Soc., 101(1), E1–E22, 2020.

Kokhanovsky, A. A., and Rozanov, V. V.: The determination of dust cloud altitudes from a satellite using hyperspectral measurements in the gaseous absorption band, Int. J. Rem. Sens., 31, Nos. 9-10, 2729-2744, 2010.

Kooreman, M. L., Stammes, P., Trees, V., Sneep, M., Tilstra, L. G., de Graaf, M., Zweers, D. C. S., Wang, P., Tuinder, O. N. E., and Veefkind, J. P.: Effects of cloud on the UV absorbing aerosol index from TROPOMI, Atmos. Meas. Tech., 13, 6407-6426, 2020.

Lorente, A., Boersma, K. F., Yu, H., Doerner, S., Hilboll, A., Richter, A., Liu, M., Lamsal, L. N., Barkley, M., De Smedt, I., Van Roozendael, M., Wang, Y., Wagner, T., Beirle, S., Liu, J. -T., Krotkov, N., Stammes, P., Wang, P., Eskes, H. J., and Krol, M.: Structural uncertainty in air mass factor calculation for NO2 and HCHO satellite retrieval, Atmos. Meas. Tech., 10, 759-782, 2017.

Nanda, S., de Graaf, M., Sneep, M., de Haan, J. F., Stammes, P., Sanders, A. F. J., Tuinder, O., Veefkind, J. P., and Levelt, P. F.: Error sources in the retrieval of aerosol information over bright surfaces from satellite measurements in the oxygen A band, Atmos. Meas. Tech., 11, 161–175, https://doi.org/10.5194/amt-11-161-2018, 2018.

Nanda, S., de Graaf, M., Veefkind, J. P., Sneep, M., ter Linden, M., Sun, J., and Level, P. F.: A first comparison of TROPOMI aerosol layer height (ALH) to CALIOP data, Atmos. Meas. Tech., 13, 3043-3059, 2020.

National Institute of Environmental Research, Geostationary Environment Monitoring Spectrometer (GEMS) Algorithm Theoretical Basis Document: Aerosol Retrieval Algorithm, 42pp, Ministry of Environment, Korea, 2020a.

National Institute of Environmental Research, Geostationary Environment Monitoring Spectrometer (GEMS) Algorithm Theoretical Basis Document: Surface Reflectance Algorithm, 35pp, Ministry of Environment, Korea, 2020b.

Park, S. S., Kim, J., Lee, H., Torres, O., Lee, K. –M., and Lee, S. D.: Utilization of O4 slant column density to derive aerosol layer height from a space-borne UV-visible hyperspectral sensor: Sensitivity and case study, Atmos. Chem. Phys., 16, 1987-2006, doi:10.5194/acp-16-1987-2016, 2016.

716 Park, S. S., Takemura, T., and Kim, J.: Effect of temperature-dependent cross sections
717   on O4 slant column density estimation by a space-borne UV-visible hyperspectral
718   sensor, Atmos. Environ., 152, 98-110, 2017.

719 Peng, J., Hu, M., Guo, S., Du, Z., Zheng, J., Shang, D., Zamora, M. L., Zeng, L., Shao,
720   M., Wu, Y. -S., Zheng, J., Wang, Y., Glen, C. R., Collins, D. R., Molina, M. J., and
721   Zhang R.: Markedly enhanced absorption and direct radiative forcing of black
722   carbon under polluted urban environments, Proc. Natl. Acad. Sci., 113, 4266-4271,
723   2016.

724 Penning de Vries, M. J. M., Beirle, S., and Wagner, T.: UV aerosol indices from
725   SCIAMACHY: Introducing the Scattering Index (SCI), Atmos. Chem. Phys., 9,
726   9555-9567, 2009.

727 Penning de Vries, M. J. M., Beirle, S., Hoermann, C., Kaiser, J. W., Stammes, P., Tilstra,
728   L. G., Tuinder, O. N. E., and Wagner, T.: A global aerosol classification algorithm
729   incorporating multiple satellite data sets of aerosol and trace gas abundances,
730   Atmos. Chem. Phys., 15, 10597-10618, 2015.

731 Prospero, J. M., Ginoux, P., Torres, O., Nicholson, S. E., and Gill T. E.: Environmental
732   characterization of global sources of atmospheric soil dust identified with the
733   Nimbus 7 total ozone mapping spectrometer (TOMS) absorbing aerosol product,
734   Rev. Geophys., 40, 1002, doi:10.1029/2000RG000095, 2002.

735 Qin, W., Fasnacht, Z., Haffner, D., Vasilkov, A., Joiner, J., Krotkov, N., Fisher, B., and
736   Spurr, R.: A geometry-dependent surface Lambertian-equivalent reflectivity
737   product for UV-vis retrievals – Part 1: Evaluation over land surfaces using
738   measurements from OMI at 466 nm, Atmos. Meas. Tech., 12, 3997-4017, 2019.

739 Rana, A., Jia, S., and Sarkar, S.: Black carbon aerosol in India: A comprehensive review
740   of current status and future prospects, Atmos. Res., 218, 207-230, 2019.

741 Sanders, A. F. J., de Haan, J. F., Sneep, M., Apituley, A., Stammes, P., Vieitez, M. O.,
742   Tilstra, L. G., Tuinder, O. N. E., Koning, C. E., and Veefkind, J. P.: Evaluation of
743   the operational Aerosol Layer Height retrieval algorithm for Sentinel-5 Precursor:
744   application to O2 A band observations from GOME-2A, Atmos. Meas. Tech., 8,
745   4947-4977, 2015.

746 Sanders, A. F. J. and de Haan, J. F.: TROPOMI ATBD of the Aerosol Layer Height
747   product, available at: http://www.tropomi.eu/sites/default/files/files/S5P-KNMI-

748   L2-0006-RP-TROPOMI_ATBD_Aerosol_Height-v1p0p0-20160129.pdf (last

749   access: 8 June 2020), 2016.

750 Sanghavi, S., Martonchik, J. V., Landgraf, J., and Platt, U.: Retrieval of optical depth

751   and vertical distribution of particulate scatterers in the atmosphere using O_2 A- and

752   B-band SCIAMACHY observations over Kanpur: A case study, Atmos. Meas.

753   Tech., 5, 1099-1119, 2012.

754 Spurr, R. "User's Guide VLIDORT Version 2.6, RT Solutions.", Cambridge, MA,

755   USA, 2013.

756 Thalman, R., and Volkamer, R.: Temperature dependent absorption cross-sections of

757   O_2-O_2 collision pairs between 340 and 630 nm and at atmospherically relevant

758   pressure. Phys. Chem. Chem. Phys. 15, 15371e15381, 2013.

759 Torres, O., Bhartia, P. K., Herman, J. R., Ahmad, Z., and Gleason, J.: Derivation of

760   aerosol properties from satellite measurements of backscattered ultraviolet

761   radiation: Theoretical basis, J. Geophys. Res., 103(14), 17099-17110, 1998.

762 Torres, O., Decae, R., Veefkind, P., and de Leeuw, G.: OMI Aerosol Retrieval Algorithm,

763   OMI Algorithm Theoretical Basis Document, Vol. III, Clouds, Aerosols and

764   Surface UV Irradiance, NASA-KNMI ATBD-OMI-03, pp. 47-71, 2002.

765 Torres, O., Jethva, H., Ahn, C., Jaross, G., and Loyola, D. G.: TROPOMI aerosol

766   products: evaluation and observations of synoptic-scale carbonaceous aerosol

767   plumes during 2018-2020, Atmos. Meas. Tech., 13, 6789-6806, 2020.

768 Vandaele, A. C., Hermans, C., Simon, P. C., Carleer, M., Colin, R., Fally, S., Merienne,

769   M. F., Jenouvrier, A., and Coquart, B.: Measurements of the NO_2 absorption cross-

770   section from 42000 cm-1 to 10000 cm-1 (238-1000 nm) at 220 K and 294 K, J.

771   Quant. Spectrosc. Radiat. Transfer, 59, 3-5, 171-184, 1998.

772 Vasilkov, A., Joiner, J., Spurr, R., Bhartia, P. K., Levelt, P., and Stephens, G.: Evaluation

773   of the OMI cloud pressures derived from rotational Raman scattering by

774   comparisons with other satellite data and radiative transfer simulations, J. Geophys.

775   Res., 113, D15S19, doi:10.1029/2007JD008689, 2008.

776 Vasilkov, A., Yang, E. -S., Marchenko, S., Qin, W., Lamsal, L., Joiner, J., Krotkov, N.,

777   Haffner, D., Bhartia, P. K., and Spurr, R.: A cloud algorithm based on the O_2-O_2

778   477 nm absorption band featuring an advanced spectral fitting method and the use

779   of surface geometry-dependent Lambertian-equivalent reflectivity, Atmos. Meas.
780   Tech., 11, 4093-4107, 2018.

781   Wang, R., Tao, S., Wang, W., Liu, J., Shen, H., Shen, G., Wang, B., Liu, X., Li, W.,
782   Huang, Y., Zhang, Y., Lu, Y., Chen, H., Chen, Y., Wang, C., Zhu, D., Wang, X., Li,
783   B., Liu, W., and M, J.: Black carbon emissions in China from 1949 to 2050,
784   Environ., Sci. Technol., 46, 7595-7603, 2012.

785   Winker, D. M., Vaughan, M. A., Omar, A. H., Hu, Y., Powell, K. A., Liu, Z., Hunt, W.
786   H., and Young, S. A.: Overview of the CALIPSO mission and CALIOP data
787   processing algorithms, J. Atmos. Oceanic Technol., 26, 2310-2323, 2009.

788   Zeng, Z. -C., Chen, S., Natraj, V., Le, T., Xu, F., Merrelli, A., Crisp, D., Sander, S. P.,
789   and Yung, Y. L.: Constraining the vertical distribution of coastal dust aerosol using
790   OCO-2 O2 A-band measurements, Remote Sens. Env., 236, 111494, 2020.

791